Performance of SHS Cement Based Composite Subjected to Blast Loading with Consideration of the Interface Properties

Jun Wu[1,2], Xuemei Liu[3,*]

[1] College of Urban Railway Transportation, Shanghai University of Engineering Science, China
[2] Department of Civil and Environmental Engineering, National University of Singapore, Singapore
[3] School of Civil Engineering and Built Environment, Queensland University of Technology, Brisbane, QLD, Australia

ABSTRACT

This paper presents the results of both experimental and numerical studies to evaluate the damage and performance of a soft-hard-soft (SHS) multi-layer cement based composite subjected to blast loading. To increase the resistance of runway pavement to blast loading, a soft-hard-soft (SHS) multi-layer cement based composite was proposed consisting of three layers including asphalt concrete (AC) reinforced with Geogrid (GST) at the top, high strength concrete (HSC) layer in the middle, and engineered cementitious composites (ECC) at the bottom layer by fully utilizing the benefits of each material. The aim is to establish a 3D numerical model to simulate this SHS composite subjected to blast loading and also validated by a full-scale filed blast test. Laboratory tests on both interface properties and strain rate effects were also conducted to characterize the material properties under dynamic loading. Modified compressive and tensile dynamic increase factor (DIF) curves were proposed for asphalt concrete based on split Hopkinson pressure bar (SHPB) and other tests. The blast resistance of the composite is evaluated in terms of the extent of damage pattern, accelerations and pressure etc against blast loading. The numerical results agreed very well with those from the blast test. Both the numerical and field blast test results showed

[*] Corresponding author. Email address: x51.liu@qut.edu.au, Fax:+61-7-3138-1170; Tel: +61-7-3138-0686.

that the SHS composite exhibited high resistance against blast loading, as per its design.

KEYWORDS: numerical model; SHS multi-layer composite; high strength concrete; blast load; dynamic increase factor; strain rate effect; interface

1. INTRODUCTION

Current runway pavement systems are designed for normal aircraft landing and taking off, and may not be adequate to provide the required resistance to blast loads arising from manmade/military bombing attacks and aircraft crashes. If the pavement is damaged, repairs must be rapid to minimize service disruptions. It is even more desirable that the extent of the damage be kept to a minimum, making rapid repair more viable. Existing pavement materials such as concrete and asphalt are not able to provide adequate resistance against blast loads. Due to their relatively brittle behaviour and limited penetration resistance, conventional pavements are not protective and damage caused by explosives might be too violent to be mitigated. As such, it is important to propose a new pavement system to sustain blast load.

Some construction materials, such as high strength concrete (HSC) (Dancygier and Yankelevsky 1996, Zhang *et al.* 2005), engineered cementitious composites (ECC) (Li *et al.* 1994, Li and Maalej 1996), and geosynthetics (GST) (Koerner 1998), have shown unique characteristics of high hardness, toughness and tensile strength. Such materials have great potential to be incorporated into a new pavement material to enhance the blast resistance of the pavement system. However, when considering the strength and weakness of each material, it is difficult for one single material to fulfil all of the requirements to resist blast load. After such consideration, a basic configuration of a multi-layer composite system was proposed to fully utilize each individual

material's benefits under blast loading. This composite system consisted of three layers, soft, hard, and another soft material layer. The "soft" material, asphalt concrete [AC], was used as a sacrificial surface layer to absorb part of the dynamic energy. Thereby greatly reducing the energy transmitted to the following layers. With the inclusion of high strength GST as a reinforcement for AC, the tensile strength of the whole AC layer was increased, which, in turn, reduced the extent of cracking and local failures within the AC layer when subjected to dynamic loading. A "hard" material was used under the AC layer, serving as the main body to sustain dynamic loads. HSC was proposed as a good candidate due to its high compressive strength. Under dynamic loading, tensile stress tends to develop at the rear face of the material due to the reflection of the compressive stress propagating from the top face. However, it is well known that HSC has a low tensile strength and is very brittle compared to conventional concrete. Therefore, another "soft" and ductile material was deemed necessary at the base of the "hard" HSC layer to absorb the reflected energy. ECC was proposed to take the soft material role in this study, as it is classed as an ultra ductile fiber reinforced cementitious composite due to its exceptional multiple cracking performance. This composite is referred to as SHS composite hereafter. As such, it is necessary to fully understand SHS composite's resistance against blast loads.

Full-scale field blast tests are time-consuming and costly. Therefore, reliable numerical simulation could be considered the best alternative. Hence, this study aimed to develop a 3D model to simulate the SHS composite using the explicit non-linear finite element program, LS-DYNA. A field blast test was undertaken and used for verification of the numerical model. For the numerical model, considering the important role of the material model in modelling different layers, the suitability of the existing material models in LS-DYNA (2007) was therefore performed. Laboratory experiments

were also conducted to validate and quantify relevant parameters. Strain rate effect was considered and dynamic increase factor (DIF) of relevant materials were also developed and incorporated into the model. Furthermore, the interface properties were investigated and verified through experiments and the results incorporated into the 3D model.

2. FINITE ELEMENT MODELLING

2.1 LS-DYNA

The numerical study on the SHS composite subjected to blast loading was performed using the LS-DYNA, an explicit finite element code dedicated to analyzing dynamic problems associated with large deformation, low and high velocity impact, ballistic penetration and wave propagation, etc. In particular, "contact algorithm" is available in LS-DYNA, which enables more accurate simulation on multi-layer materials like SHS composite by considering the interface performance.

2. 2 Material model

In this numerical model, 6 types of materials needed to be modelled: the ECC layer, HSC layer, AC layer, GST, steel bar and foundation soils. The first 3 materials (ECC, HSC and AC) can be grouped as concrete material.

2.2.1 Concrete damage model

When subjected to blast loading or high impact loading, concrete or other similar materials have shown a highly non-linear response. They usually exhibit pressure hardening and strain hardening under static loading, and strain rate hardening in tension and compression under dynamic loading. A number of material models have been developed to model concrete recently (Holmquist *et al.* 1993, Malvar *et al.* 1997, Polanco-Loria *et al.* 2008, Riedel *et al.* 2009). Among them, the MAT72 model has

been widely used to analyse concrete response to blast loading due to its simple implementation. In addition, the MAT72 R3 model can capture the non-linear behaviour of the material under dynamic loading (Malvar *et al.* 1997). Therefore, the MAT72 R3 was adopted in this study to simulate concrete and/or other similar materials including AC, HSC, and ECC. The key features of the model are discussed briefly in the following section.

Strength surface in MAT72 R3 model

The MAT72 R3 model has three independent strength surfaces: "maximum strength surface", "yield surface" and "residual strength surface", shown graphically in Figure 1. During the initial increase of hydrostatic pressure P, the deviatoric stresses $\Delta\sigma$ remains in the elastic region until the "yield surface" is reached. Deviatoric stress can be further developed until the "maximum strength surface" is reached, and the material will subsequently start to fail. After failure is initiated, the material will gradually lose its load carrying capacity and reach its "residual strength surface".

Damage factor in MAT72 R3 model

After reaching the initial "yield surface" but before reaching the "maximum strength surface", the current surface can be obtained as a linear interpolation between "yield surface" $\Delta\sigma_y$ and "maximum strength surface" $\Delta\sigma_m$:

$$\Delta\sigma = \eta(\Delta\sigma_m - \Delta\sigma_y) + \Delta\sigma_y \qquad (1)$$

After reaching the "maximum strength surface" the current failure is interpolated between the "maximum strength surface" $\Delta\sigma_m$ and the "residual strength surface" $\Delta\sigma_r$ which is similar to the above computation:

$$\Delta\sigma = \eta(\Delta\sigma_m - \Delta\sigma_r) + \Delta\sigma_r \quad (2)$$

where η varies from 0 to 1 depending on the accumulated effective plastic strain parameter λ. The value of η normally starts at 0 and increases to unity at $\lambda = \lambda_m$ and then decreases back to 0 at some larger value of λ. λ_m is the plastic strain at "maximum strength surface". The accumulated effective plastic strain λ can be expressed as follows:

$$\lambda = \int_0^{\bar{\varepsilon}^p} \frac{d\bar{\varepsilon}^p}{r_f[1 + p/(r_f f_t)]^{b_1}} \quad \text{for } p \geq 0 \quad (3)$$

$$\lambda = \int_0^{\bar{\varepsilon}^p} \frac{d\bar{\varepsilon}^p}{r_f[1 + p/(r_f f_t)]^{b_2}} \quad \text{for } p < 0 \quad (4)$$

where f_t is the quasi-static tensile strength, $d\bar{\varepsilon}^p$ is effective plastic strain increment, r_f is the dynamic increase factor (DIF) of the material under dynamic loading. The damage factors b_1 and b_2 define the softening behaviour due to compression ($P \geq 0$) and tension ($P < 0$), respectively. Parameter b_1 can be determined by considering compressive energy G_c (area under compressive stress-strain curve) obtained from uniaxial compression test in single element simulation. It is obtained iteratively until the area under stress-stain curve from single element simulation coincides with G_c / h, where h is the element size. Then b_2 is determined by considering fracture energy G_f from uniaxial tensile test or three points notched beam test in single element simulation. The value of b_2 is obtained until the area under tensile stress-stain curve from a single element coincides with G_f / w_c, where w_c is the localization width, and typically w_c is

taken as 1 to 6 times the maximum aggregate size (Malvar *et al.* 1997).

Based on Equations 2 and 4, the stress softening factors η and λ were governed by the accumulation of effective plastic strain. However, when the stress path was very close to the negative hydrostatic pressure axis, i.e. isotropic tension, wherein the hydrostatic pressure would decrease from 0 to $-f_t$, where no deviatoric stress occurred, no damage accumulation would have occurred based on these equations. However, in such "concrete-like" materials damage could not be avoided even at this state. Therefore, the above condition had to be modified by including pressure-softening effects near or after tensile failures. In this case, a volumetric damage increment was calculated and added to the total damage factor λ whenever the stress path was close to the triaxial tensile path.

A scaled damage indicator δ was proposed to describe the damage level of the material in this paper. The scaled damage indicator δ can be expressed as:

$$\delta = \frac{2\lambda}{\lambda + \lambda_m} \qquad (5)$$

in which, λ is accumulated effective plastic strain as defined in Equations 3 and 4.

It should be noted that there were three threshold values in Equation 5: (i) at "yield surface", $\lambda = 0$, leading to $\delta = 0$; (ii) at "maximum strength surface", $\lambda = \lambda_m$, leading to $\delta = 1$; and (iii) at "residual strength surface", $\lambda = \lambda_r$ □ λ_m, leading to $\delta = 1.99 \approx 2$. Thus the varied δ value from 0 to 1 and then to 2 indicated that the failure surface migrated from "yield surface" to "maximum strength surface" and then to "residual strength surface" respectively, as the material was being stressed.

As this research focused on both the initiation and the degree of damage to the "concrete-like" material subjected to blast loading, the post-peak behaviour was of great interest. Thus, such post-peak behaviour obtained from FEM modelling was plotted for the δ value from 1 to 2. The higher δ value represented the higher degree of damage. In this study, it was further assumed that the threshold δ value classified for the "severe crack" situation was 1.8, i.e. when δ value reached 1.8 and beyond, the material was considered severely damaged.

Strain rate effect

The material model MAT 72 R3 also included a radial rate enhancement on the material failure surface. This is because experimental data for "concrete-like" materials were typically obtained along radial paths from the origin in deviatoric stresses versus hydrostatic pressure via unconfined compressive and tensile tests.

Equation of State (EOS)

In addition to the strength surface model, an equation of state (EOS) is needed to describe the relationship between hydrostatic pressure and volume change of the material subject to dynamic load. EOS is usually determined using a fly impact (i.e. for steel) test or triaxial compressive test (i.e. for concrete or geomaterials). The isotropic compression portion of the MAT72 R3 material model consists of pairs of hydrostatic pressure P and corresponding volume strain μ. It was implemented as a piece-wise curve in this study.

2.2.2 GST and Steel

GST and steel were modelled using a "plastic-kinematic" model, a elastic-fully plastic model with kinematic hardening plasticity, in accordance with Von Mises yield

criterion. The Von Mises yield criterion assumed that the initial yield or failure surface was independent of the hydrostatic stress and the third invariant of the deviatoric stress (Holmquist *et al.* 1993). Hence, it resulted in a circular shape with constant radius in deviatoric plane and similar values for uniaxial yield tensile stress and uniaxial yield compressive stress (Chen 1982).

2.2.3 Foundation soil material

The foundation soil was modelled using a "Drucker-Prager" model, in which the cohesion and compaction behaviour resulted in an increasing resistance to shear until a limit value of yield strength as the pressure increases (Chen 1982). Depending on the matched stress states, the material constants are related to the constants c and φ of the Mohr-Coulomb criterion in several ways (i.e. match along compressive meridian or tensile meridian).

2.3 Interface model

The "interface model" was used for multi-layer composite systems, especially between AC and HSC layer. The TIEBREAK contact algorithm was used to simulate the interface behaviour between HSC and AC layers because it allowed simulation of crack propagation at the interface. The stress-displacement response depends on the energy release in the separation process of the interface. The simplest form of stress-displacement had a linear elastic response until the crack initiation criterion was reached and was then followed by a linear softening to zero stress when the damage was fully reached (LS-DYNA 2007). The area under the stress-displacement curve was the "energy released rate", which described the energy dissipation during the development of crack at interface.

The interface element was considered "failed" based on damage evolution. Damage is defined as a linear function of the distance between points initially in contact. When the distance exceeds the defined critical distance, the interface is considered completely failed. Thus, the energy release rates G_I and G_{II} for normal and shear interface failure modes were defined as:

$$G_I = \frac{1}{2}\tau_n \square D \qquad (6)$$

$$G_{II} = \frac{1}{2}\tau_s \square D \qquad (7)$$

where, τ_n and τ_s are the normal stress and shear stress at the interface, D is the critical displacement for total failure.

Tensile (pullout test) and direct shear tests were conducted to obtain the energy release rate G_I and G_{II}. It should be noted that the value τ_n and τ_s was related to the characteristic element length (square root of area at interface). Usually, the low failure stress value was needed for coarser meshes. Hence, τ_s and D could first be numerically determined by matching the load-displacement curve from the direct shear test, and then τ_n could be obtained by the known value of D and G_I via Equation 6. After the failure criterion was met, the nodes were separated. The interface then behaved the same as the surface-to-surface contact type which transferred the shear stress and compressive stress at the interface.

3. DETERMINATION OF MATERIAL MODEL PARAMETERS

This section summarises the key parameters for the material models in modelling the innovative SHS multi-layer pavement composite under blast loading.

3.1 AC layer

The MAT72 R3 model was employed to simulate AC to capture post-peak behaviour. This model did not consider the temperature effect. However, during the blast event, the temperature suddenly increased to a thousand degrees in a few microseconds, and then dropped quickly with propagation distance. Based on the field test, only the central part of the AC layer was destroyed under the combined effects of high temperature and blast pressure. With the increase in distance from the centre, the failure of the central AC surface was mainly due to blast pressure, and the high temperature effect could be ignored. Therefore, the MAT72 R3 material model for AC was used in this research.

3.1.1 Strength Surface

As mentioned in section 2.2, the MAT72 R3 material model had three strength surfaces: strength, residual strength, and yield surfaces. These three surfaces can be obtained through curve fitting of suitable experimental data. Available data was extracted from Park *et al.* 2005 with the compressive strength f_c=0.311 MPa for AC. Figure 2 presents the determination of the three surfaces by curve fitting for AC with f_c=0.311 MPa. The intersection point of maximum strength surface and residual strength surface was the brittle-to-ductile point. This point should be determined by experimental data under high confining pressure. However, it was difficult to determine this point in strength surface as no experimental data was available for AC. Based on the experimental data for concrete, this point was usually taken as p/f_c=3.878. Considering the size and strength of aggregates used in AC and concrete was almost the same, the brittle-to-ductile point for AC was taken to be the same as that for concrete. This value may be conservative for AC due to the higher content of coarse aggregate

mixed in asphalt mixture. However, in terms of the simulation results, this value could be acceptable. In this study, the unconfined compressive strength for AC in field trial test was 4.6 MPa, and the tensile strength was 0.7 MPa at 35°C. By scaling the data from the established curves given in Figure 2, the appropriate strength surface of the current materials can be determined as shown in Figure 3.

3.1.2 Damage factor

The strain hardening and softening pairs (η, λ) in Equations 1 and 2 described the material behaviour transmitted from "yield surface" to "maximum strength surface" and from "maximum strength surface" to "residual strength surface", respectively. During the transmission, parameter η varied from 0 to 1 depending on the accumulated effective plastic strain parameter λ. However, it was found that the original damage factor pairs (η, λ) in the MAT72 R3 model were only suitable for concrete and not for the AC material due to AC having higher plastic failure strain. Thus, the input for accumulated effective plastic strain λ was modified. Based on the uniaxial compressive test for AC, it was found that at peak stress the corresponding strain was approximately 0.018 and the final failure strain was about 0.1. While for normal concrete, the corresponding strain at peak stress was around 0.0022. Hence, the λ was modified to give the high failure strain for AC. Additionally, it was found that when λ was adjusted to 10 times the original λ value the numerical results seemed to show good agreement with experimental results from unconfined compressive test for AC. Figure 4 shows the modified and original series of (η, λ) pairs. It can be seen that the modified damage factor made smoother descending than the original damage factor, and had a higher failure strain that seemed to match the behaviour of AC very well.

3.1.3 Equation of state

There were limited EOS data for AC. The available EOS data is for AC with compressive strength of f_c=3.8 MPa (Tang *et al.* 2009). In this study, the compressive strength for AC was f_c=4.6 MPa. Thus, the pressure-volume pairs were calculated using the scaling method (Malvar *et al.* 1996). In this method, assuming that new data would be obtained at the same volumetric strains, and thus the new corresponding pressure (pc_{new}) would be:

$$pc_{new} = pc_{old}\sqrt{r} \quad (8)$$

and the new corresponding unloading bulk modulus (ku_{new}) would be:

$$ku_{new} = ku_{old}\sqrt{r} \quad (9)$$

where r is the scaling factor which is the ratio of compression strength for new material to compression strength of the previous material modelled. Hence, the EOS data for f_c=4.6 MPa was calculated based on Equations 8 and 9 as shown in Figure 5.

3.1.4 Softening parameter b_1, b_2

The softening parameters (b_1, b_2) shown in Equations 3 and 4 controlled the material softening behaviour after peak stress. These parameters were obtained from experiments, as detailed below.

A) Value of b_1 from uniaxial compressive test

The uniaxial compressive test was conducted for AC according to ASTM 1074. The compression testing results are presented in Figure 6. It was found that the

corresponding strain at peak stress (f_c=4.6 MPa) was about 0.018 and the final failure strain was about 0.1, which was higher than that of concrete. The Young's modulus obtained from stain gauges attached at the middle height of the sample was 598 MPa. Based on experimental results, the compressive energy G_c was calculated at 15.1 MPa·mm. Hence, b_1 for different element sizes were obtained through single element simulation as suggested in section 3.1. The b_1 value for 10 mm mesh size was found to be 4.2.

B) Value of b_2 from fractural test

The value of b_2 was determined by fracture energy G_f, which can be obtained from uniaxial tensile test or three points Single-edge Notched Beam test (SNB). In the current study, the SNB test was carried out to evaluate fracture energy G_f for AC. Detailed theory about the SNB test can be found in established literature (Karihaloo and Nallathambi 1990). Therefore, only the test result is presented here. In the SNB test, the compacted AC beam was fabricated with a dimension of 400×100×100 mm^3 depth. A mechanical notch was sawn with a depth of 20 mm, which gave a ratio of notch to beam depth of 0.2. The simply supported sample with a span length of 340 mm was tested under 35°C temperature. From the test, fracture toughness K_{IC} was obtained according to the formula suggested by Karihaloo and Nallathambi (1990). Then the fracture energy G_f was calculated using:

$$G_f = \frac{\left(1-v^2\right)K_{IC}^2}{E} \quad (10)$$

in which E is the elastic modulus and v is possion's ratio.

b_2 was obtained via iterative procedure until the area under stress-stain curve from single element simulation coincided with G_f / w_c. The parameters obtained from SNB and single element simulation for AC (f_c=4.6 MPa) are summarized in Table 1.

3.1.5 Strain rate effect for asphalt material

Dynamic increase factor for compression

In the current study, DIF for AC under different strain rate was obtained using servo hydraulic fast loading tests and the split Hopkinson pressure bar (SHPB) test. The strain rate produced by the servo hydraulic machine was approximately 10^{-5} to 1 s^{-1}, and the higher strain rate loading was obtained through SHPB testing.

The DIFs for AC under different strain rate from SHPB and the servo hydraulic machine test is illustrated in Figure 7. It shows that the DIF increased with the increase of strain rate. Moreover, the DIF value increased sharply at a certain strain rate, which was similar to the behaviour of the "concrete-like" material. The fitted curve of the AC's DIF data had two segments, with a threshold point at $100s^{-1}$. For strain rate less than $100s^{-1}$, it was in a monotonic increasing trend, while it was a straight line with strain rate exceeding $100s^{-1}$. Hence, the dependence of DIF on strain rate for AC under compression ($DIF_{AC,c}$) was proposed as following piece-wise functions:

$$DIF_{AC,c} = \frac{f_d}{f_s} = 3.18 + 1.098\log_{10}(\dot{\varepsilon}) + 0.1397\log_{10}{}^2(\dot{\varepsilon}) \quad \text{for } \dot{\varepsilon} \le 100s^{-1} \tag{11}$$

$$DIF_{AC,c} = \frac{f_d}{f_s} = 21.39\log_{10}(\dot{\varepsilon}) - 36.76 \quad \text{for } 100s^{-1} < \dot{\varepsilon} \le 200s^{-1} \tag{12}$$

A numerical modelling of the SHPB test adopting this DIF curve found that the initial segment of this curve matched the experimental results very well, while the

numerical model results for strain rate larger than $100s^{-1}$ seemed to overestimate the stress. This could be due to the "double counting" of the inertia effect in the numerical modelling when strain rate exceeded $100s^{-1}$. Hence, in the current model, the second segment was ignored when the strain rate exceeded $100s^{-1}$. Beyond this, the DIF was assumed to remain a constant value.

Dynamic increase factor for tension

For the high strain rate in tension, the SHPB setting was employed for conducting the dynamic splitting tensile test. The servo hydraulic machine was also used to conduct dynamic splitting tensile testing for a low to moderate strain rate range. The configuration of the test and sample information can be found in Wu (2012). The test results are presented and discussed here. The test results for dynamic tensile strength of AC are shown in Figure 8. From the figure, it can be seen that the splitting tensile strength increased with the increase of the strain rates following a bi-linear trend. The transition point was found to be at $15s^{-1}$. The post-experimental picture revealed that the binder failure and trans-aggregate failure had occurred at about 15 to $80s^{-1}$, consistent with observations from Tekalur *et al.*(2009). The stress wave within the specimen went through the aggregated or binder material under dynamic loading while under the static loading, the failure usually occurred at the weakest component (interfacial zone) within the specimen. The dependence of DIF on strain rate for AC under tension ($DIF_{AC,t}$) was proposed based on experimental results as following piece-wise functions:

$$DIF_{AC,t} = \frac{f_d}{f_s} = 1.86 + 0.1432\log_{10}(\dot{\varepsilon}) \quad \text{for } \dot{\varepsilon} \le 15s^{-1} \tag{13}$$

$$DIF_{AC,t} = \frac{f_d}{f_s} = 6.06\log_{10}(\dot{\varepsilon}) - 5.024 \quad \text{for } 15s^{-1} \le \dot{\varepsilon} \le 100s^{-1} \tag{14}$$

In the macro-level numerical model, the MAT 72R3 material model cannot capture the aggregate interlocking that propagates the micro-cracking and energy dissipation beyond the localization zone (Magallanes *et al.* 2010). Therefore, the above proposed tensile DIF curve with two branches was used in the model.

3.2 HSC and ECC layer

The MAT72 R3 model was also used to simulate HSC and ECC. The parameters for HSC are illustrated in Table 2. For HSC, the equation recommended by CEB (Comite Euro-International du Beton 1993) was adopted to consider the dependence of DIF on strain rate. However, similar to the above-mentioned AC material, only the first segment of the compressive DIF curve for concrete-like material was employed in the present study. The tensile and compressive DIF curves used for the numerical model are shown in Figure 9.

The ECC was first simulated by Lee (2006) using the MAT 72 R3 model, and it showed that such a material model was suitable for modelling ECC material under dynamic loading, including impact and blast loading. Hence, the MAT72 R3 was used to simulate ECC in this study. The material properties of ECC are given in Table 2. The DIF curve for ECC under compression and tension were recommended by Lee (2006) and Maalej *et al.* (2005), respectively. Both tensile and compressive DIF curves for ECC used in the model are shown in Figure 10.

3.3 GST and Steel

A) GST

Geosynthetics reinforcement may enhance the tensile strength of the AC layer, Therefore, it is necessary to consider the function of the GST material. In the current study, the GST reinforcements were simulated with shell element formulation in LS-DYNA due to its computational efficiency. The thickness of the shell element was taken as the average between the rib and the junction thickness (Lee *et al.* 2010). Since the GST showed the bilinear stress-strain behaviour, where some hardening behaviour had taken place after the initial yield point P as shown in Figure 11. The plastic-kinematic model was employed to simulate the behaviour of GST. The parameters for GST in the plastic-kinematic model were determined by fitting the bilinear curve with experimental load-strain curve, shown in Figure 11. The parameters for GST used in this simulation are summarized in Table 3.

B) Steel bar

A steel bar is an isotropic material having the same initial yield stress for both uniaxial tension and uniaxial compression. The plastic-kinematic model was suitable to model isotropic and kinematic hardening plasticity. Thus, the plastic-kinematic model was employed to describe the behaviour of the steel bar in this study. The material parameters of the steel bar in this study are summarized in Table 3.

3.4 Foundation soil

The Drucker-Prager model was used to model the subgrade soil foundation. The soil parameters in the model are estimated from actual soil investigation performed on the test site (Wang *et al.* 2010) as shown in Table 4.

3.5 Interface properties

For the SHS composite, it was assumed that the HSC and ECC were fully bonded, while the interface between HSC and AC was weaker than that between HSC and ECC. This was mainly due to the construction method's difference as the AC layer was directly placed on the HSC layer a few days after HSC casting. Strain and stress can be transferred between AC and HSC when vertical and horizontal loading is applied on the AC layer. The interfacial shear strength between AC and HSC can influence the integrity of the stress/strain transfer. Therefore, laboratory investigations were conducted to obtain interface properties between the HSC and AC layers.

3.5.1 Shear strength and static friction coefficient

A direct shear test method was adopted to investigate the shear behaviour between AC and HSC. The configuration of the test is presented in Figure 12. The direct shear test was conducted under constant vertical loading and four levels of vertical loading were applied: 2.1 MPa, 1.5 MPa, 1 MPa and 0.5 MPa. The maximum tire pressure -2.1MPa from typical military and civilian aircraft was set as the maximum vertical loading in the direct shear test.

The results from the direct shear test are shown in Figure 13. It clearly shows that the shear strength for interface was around 1.5 MPa for the maximum normal loading 2.1 MPa. This value was set as the maximum shear strength for the current interface between AC and HSC. At the failure surface, it was found that the asphalt surface was smashed during the shear test, while the HSC surface had less damaged than that of asphalt surface. Shear failure was mainly due to the failure of the AC surface. It was found that the static friction coefficient of the AC and HSC interface was 0.71, or a friction angle of 35°.

3.5.2 Dynamic friction coefficient

Dynamic friction is defined as the frictional force between two moving solid surfaces in contact with each other. Where the objects are in motion, there will still be frictional force. Usually, the dynamic friction coefficient was lower than the static friction coefficient. A tilt table test was used to evaluate the dynamic friction coefficient. The theory of the tilt table test is shown in Figure 14. In the figure, it is assumed that the solid body was sliding along the tilt surface with certain acceleration. The weight of solid body is mg, the tilt angle from the horizontal surface is θ. For the solid body, the force along tilt surface from its own weight is expressed as $mg\sin\theta$, the component normal to the tilt surface is $mg\cos\theta$. Considering the equilibrium of force normal to the tilt surface, the reaction force R equals to $mg\sin\theta$. Thus the dynamic friction F is expressed as $\mu_{dynamic} mg\cos\theta$. The total sliding force along the tilt surface is then expressed as $(mg\sin\theta - \mu_{dynamic} mg\cos\theta)$. Hence, according to the Newton's second law $F = ma$, the acceleration of solid body can be expressed as:

$$a = g(\sin\theta - \mu_{dynamic}\cos\theta) \tag{15}$$

If the acceleration is zero, meaning that the solid body is sliding along the tilt surface with constant velocity, based on the Equation 5.1, the dynamic friction coefficient can be resolved as:

$$\mu_{dynamic} = \frac{\sin\theta}{\cos\theta} = tg\theta \tag{16}$$

It can be seen that the dynamic friction coefficient can be directly obtained from the tilt angle, when the rigid body object is sliding at a constant speed down the slope.

The set-up to evaluate the dynamic friction coefficient between the HSC and AC layers is shown in Figure 15. The AC block was placed along the tilt surface, made of HSC material. The tilt angle was adjusted to make the AC block slide along the surface with constant velocity, from which the friction coefficient was derived. With a few tests, the dynamic friction angle between AC and HSC layer was found to be about 29° to 30°. Hence, the dynamic friction coefficient was between 0.55-057. According to the result of the direct shear test, the static friction coefficient between AC and HSC was around 0.71, which corresponded to the friction angle of 35°. It was found that the dynamic friction coefficient was about 78% of the static friction coefficient. In the current study, the dynamic friction coefficient is taken as 0.56.

3.5.3 Interface model validation

The simulation of the direct shear test using TIEBREAK contact was validated using the direct shear test conducted above. The size of the model was taken as the same as that in the laboratory test. Solid element was used to model AC and HSC material. The TIEBREAK contact algorithm was employed to simulate the interface behaviour. The parameters for interface simulation are listed in Table 5. The load-displacement curve obtained from the simulation was compared with the experimental result and it was found that both peak shear force and the corresponding displacement at peak shear force from the numerical model agreed well with that obtained from the experiments. Therefore, the TIEBREAK contact in LS-DYNA was confirmed as capable of modelling the interface behaviour of HSC and AC and was used for the 3D simulation.

4. FULL SCALE BLAST TEST

One SHS multilayer pavement composite slab was designed and tested in the field under blast loading. A bomb the equivalent of a 7.3kg TNT charge weight was

placed at the centre of the slab, with the bomb's centre of gravity elevated at 170 mm above the slab surface. This multi-layer pavement slab was cast on site with a dimension of 2.8×2.8×0.275 m^3. Figure 16 shows the cross-sectional view of this slab. A 100mm thick ECC layer was placed at the bottom of the slab. Another 100mm thick HSC layer was constructed above the ECC layer before it was completely hardened in order to improve the interface bonding. These two bottom layers were allowed to cure for one week, and then the third AC layer was cast on the top of the existing two layers. The AC layer was cast in two sub-layers with a thickness of 38mm for each. Both layers were compacted using a small 1-tonne compactor. A GST layer was placed in-between the two asphalt sub-layers as reinforcement for the AC layer. The GST was Polyfelt Microgrid MG-100 with bi-directional tensile strength at 100 kN/m and had an aperture size of 7 mm.

To facilitate the lifting and transportation of the completed slabs to the site, minimal reinforcements -T12 steel bars in both directions at about 350mm spacing, with a cover of 25mm were installed in the bottom ECC layer. This reinforcement was undertaken to prevent the pavement slab from cracking under its own weight during transportation. To simulate an actual pavement condition, which is much wider and with sufficient side anchorage, the pavement slab was anchored to the ground. Thus, four vertical anchors were installed near the corner of the pavement slab. Figure 17 shows a photograph of the completed pavement slab with four anchors.

Various instruments were installed onto the slab to measure its responses during blast loading. Figure 18 shows the instrumentation installed on the pavement slab. Four accelerometers were installed at the middle of the side of the slab to measure both vertical (V1 and V2 in Figure 18) and horizontal accelerations (H1 and H2 in Figure 18). The accelerometers were mounted onto steel frames that were cast together with

the slab. Three total pressure cells (TPC) (TPC1, TPC 2 and TPC3 in Figure 18) were buried in the soil just below the slab to measure the pressure transferred from the pavement slab. The measurement results of the field blast testing will be discussed and compared with the numerical simulation results in section 5.

5. MODELLING SHS COMPOSITE UNDER BLAST LOADING

5.1 Model development

The multi-layer slab and soil mass were discretized in space with one point gauss integration eight-node hexahedron Lagrange element. Only a quarter of the slab was modelled considering symmetry. Thus, the dimension of the slab in the numerical model was 1400×1400×275 mm^3. Regarding the soil domain, with mesh size convergence analysis, the thickness and length of soil mass were taken as 5600 mm and 7000 mm, respectively.

The reinforcement bars and GST were spatially discretized using beam element and shell element, respectively. It was assumed that the reinforcement bars and GST were fully bonded within the ECC and AC (in the field blast test, the rebar was placed in the layer of ECC, and the GST was placed in the AC layer). The anchors on the multi-layer pavement slab were also considered and simulated as fixed points in the corresponding position in the numerical model. The soil mass was treated as a semi-infinite space. Thus, the non-reflection boundary was applied on the side and bottom of the soil mass. The Automatic_Surface_To_Surface contact algorithm was employed to simulate the interaction between the pavement slab and the soil mass.

The element cells for the pavement slab had an aspect ratio of 1, suitable to simulate wave propagation. Due to the computational time and capability, “bias mesh technology” was adopted for the soil mass. In the central part of the soil mass under the

pavement slab, the mesh size was uniform with an aspect ratio of 1. The mesh size was gradually increased away from the centre part of the soil mass, both radially and vertically. After the convergence study, it was found that a 10 mm element size in the centre part of the slab gave stable and accurate results.

LS-DYNA uses a commonly used blast load routine CONWEP (Hyde 1992) to generate blast loadings. It should be noticed that the blast pressure from CONWEP were well calibrated using many full scale field tests by the US Army. The minimum scaled distance (scale distance = [distance between bomb and target] / [TNT charge weight of bomb]$^{1/3}$) in CONWEP is around 0.15 m/kg$^{1/3}$, meaning that the blast pressure would be accurate when the actual stand-off scaled distance is larger than this threshold value. This can be classified as a middle to far field blast range. However, when the scaled distance is smaller than this value (i.e. close-in blast range), the blast pressure generated in CONWEP is obtained through extrapolation from the blast pressure at 0.15 m/kg$^{1/3}$ scaled distances, which may not be accurate enough. In this study, the charge weight of 7.3 kg equivalent TNT was placed 170 mm above the slab. Thus, the scaled distance was 0.087 m/kg$^{1/3}$, and the blast pressure obtained from the CONWEP model might not be accurate. Furthermore, the CONWEP method adopted the planar blast wave front when the blast wave reached the target, which means that the whole target was subjected to a uniform magnitude of blast pressure. This simplified method is acceptable when the target is relatively small. However, in the current study, the target was a large piece of pavement slab. During the blast event, the blast pressure exerted on the slab would be a function of distance and time of arrival, therefore, to more accurately model such blast pressure, a 3D computational fluid dynamic (CFD) program called AUTODYN was used in this study. The blast pressure was extracted from AUTODYN and then applied onto the slab model target in LS-DYNA. The detailed

process of applying pressure to the pavement surface can be found in Wu and Chew (2014).

5.2 Simulation results

The results of the numerical modelling of the SHS pavement composite under blast loading, with the incorporation of the above-mentioned material models, are summarized and discussed in this section. The simulation results are compared with the blast test results and discussed below.

The damage situation for new multi-layer pavement slab in field blast test is shown in Figures 19 and 20. Figure 19 shows that the blast pressure destroyed the upper half of the asphalt layer above the GST reinforcement. It was also noted that only the centre of the GST piece was burned off during the blast event. Figure 20 shows the resulting damage on the HSC layer after removing the top layer of asphalt. From this figure, it can be seen that the crater was very shallow and did not punch through the whole layer and a crater of around 700mm diameter and depth of 10mm was formed on the HSC layer.

The results of the damage situation for new multi-layer pavement slab using the numerical model are given in Figure 21. The “fringe level” in the contour is the value for scaled damage indicator δ, which is defined in Equation 5. When the δ value is greater than 1.8, the material is considered severely damaged. The damagepattern for AC layer is shown in Figure 21(a). Comparing Figure 21(a) and Figure 19, it is observed that the damage pattern in the numerical model is symmetrical while that in the field measurement is skewed. This is because the bomb in the field was not placed at the centre of the slab, and one side of the asphalt was more severely damaged than the other. Shear cracking near the anchor point was observed in the numerical model, which

was similar to the experimental observations in the field test. It could be concluded that the basic failure pattern given by the numerical model agreed well with the results obtained from the field-testing.

Figure 21(b) shows the damage pattern for the HSC layer. Comparing Figure 21(b) with Figure 20, the damage pattern for HSC was very consistent between field measurement and numerical results. The diameter of the crater was about 750mm in the numerical model, which was quiet close to that of the blast test result. As shown in Figure 21(b), shear cracks were also observed near the anchor points. Based on the damage pattern in the field blast test, the crater on the top face of the HSC was shown to be shallow and with a thickness of less than 10mm. However, after cracking occurred at the bottom face of the HSC layer, the numerical model showed that the bottom of the HSC had experienced severe cracking. This might be due to the combination of the bending of the HSC layer under blast load and the reflection of the stress wave at the bottom interface. In the numerical model, the interface between HSC and ECC was assumed to be fully bonded. However, ECC is more flexible than HSC, and thus it would cause tensile stress at the bottom face of HSC layer when deformed together. The compression stress wave from the top face would also travel within the HSC layer and reflect as a tension stress at the interface, which could cause spalling. Based on the damage pattern in the numerical model, the HSC layer may be considered failed, while the field observation may suggest that HSC was partially failed.

Figure 21 (c) shows the damage pattern the for ECC layer. As shown in the figure, only small amounts of moderate cracks were found at the centre of the top face of the ECC layer. Some severe cracks were found at the bottom face but all within a very limited area. Field observation of the ECC layer showed that it was still intact and functional.

Above all, in terms of the damage pattern, the behaviour of the SHS composite under blast loading was well predicted by the numerical model. For this multi-layer composite, only the top AC layer required major repair or replacement, while the HSC layer needed minor repair. The bottom ECC layer can be considered undamaged. This indicates the advantage of using the proposed multi-layer system.

In the blast testing, four accelerometers were installed at the mid-side of the pavement slab to measure the vertical and horizontal acceleration of the pavement slab subjected to blast loading. For the horizontal acceleration, the horizontal acceleration readings on the two sides were not the same due to the centre of the charge (conical shape) being closer to one side of the pavement slab. While in the numerical model, it was assumed that the explosion occurred in the centre of the pavement slab. Thus, in this section, only the vertical acceleration from the field blast test was compared with that of the numerical model.

The vertical acceleration from the blast testing was compared with that of numerical model as shown in Table 6. The results from both the blast testing and the numerical simulation were comparable. The maximum difference of vertical acceleration between the blast testing and the numerical model was about 10%, and the numerical model predicted slightly higher in vertical acceleration than that of the blast test.

The pressure values in the corresponding points in the numerical model were compared with pressures obtained from the blast test, as summarized in Table 7. The pressure values from the numerical simulation were shown to be close to that from the blast test for TPC2. While for TPC3, it showed a 20% discrepancy, which was acceptable in the numerical simulation considering the inherent variation in the blast

test.

TPC1 was damaged during the blast test, and no pressure reading was recorded from it. The numerical model predicted the pressure might be as high as13 MPa at that point which was far beyond the maximum measurement capacity of the pressure cell installed. That could explain why TPC1 was destroyed due to the overwhelming blast loading.

6. CONCLUSIONS

A 3D numerical model was developed to model the behaviour of the innovative SHS multi-layer pavement composite under blast loads. The SHS composite included three layers; one layer of GST reinforced asphalt on the top, one layer of engineered cementitious composites (ECC) at the bottom, and another layer of high strength concrete (HSC) in between. The concrete damage model in LS-DYNA was adopted for modelling. The modified damage factor proposed in this paper made smoother descending than the original damage factor, and had a higher failure strain that could improve the simulation of the behaviour of AC. Contact algorithm was incorporated to simulate the behaviour of the interfaces. The key parameters for the material models were all verified according to a variety of experiments. In particular, interface properties between HSC and AC were considered and the model was validated through laboratory experiments. Moreover, the strain rate effects were also added into the model. Modified compressive and tensile DIFs for asphalt concrete were also proposed with consideration of the strain rate effects, based on the results obtained from the SHPB tests.

Using the developed model, the performance of the innovative SHS composite subjected to blast loading was simulated and compared to the corresponding blast test

rests. The damage pattern of the SHS composite under blast loading compared with that obtained in the blast test was well predicted by the numerical model. The vertical acceleration response from the numerical simulation was also comparable to that from the blast testing. In addition, the pressure values from the numerical model were also reasonably consistent with the pressures measured from the blast tests though the numerical model predicted slightly higher than that from the blast test. In addition, Both the numerical and field blast test results showed that the SHS composite exhibited high resistance against blast loading, as per its design.

ACKNOWLEDGEMENTS

This research is funded by Defence Science and Technology Agency (DSTA), Singapore, Grant No.CN07001904, through the Centre for Protective Technology, National University of Singapore. The authors are grateful to Dr. Zhiwei He and Dr. Andy Hong Wei Tan for their assistance on the experiment work.

REFERENCES

Chen, W.F. (1982). *Constitutive equations for engineering materials*: John Wiley & Sons.

Comite Euro-International Du Beton, 1993. Cep-fip model code 1990. Redwood Books, Trowbridge, Wiltshire, UK.

Dancygier, A.N. & Yankelevsky, D.Z. (1996). High strength concrete response to hard projectile impact. *International journal of Impact Engineering,* 18 (6), 583-599.

Holmquist, T.J., Johnson, G.R. & Cook, W.H. (1993). A computational constitutive model for concrete subjected to large strains, high strain rates, and high pressures. *The 14th International Symposium on Ballistics.* Quebec, Canada, 591-600.

Hyde, D. (1992). *Conwep-application of tm5-855-1. Fundamentals of protective design for conventional weapons.* Vicksburg, MS.

Karihaloo, B.L. & Nallathambi, P. (1990). Effective crack model for the determination of fracture toughness (k_{ic}^{e}) of concrete. *Engineering Fracture Mechanics,* 35 (4/5), 637-645.

Koerner, R.M., 1998. *Designing with geosynthetics* N.J.: Prentice-Hall Eaglewood.

Lee, K.Z.Z., Chang, N.Y. & Ko, H.Y. (2010). Numerical simulation of geosynthetic-refinforced soil wall under seismic shaking. *Geotextiles and Geomenmbranes,* 28, 317-334.

Lee, S.C. (2006). *Finite element modeling of hybrid-fiber ecc targets subjected to impact and blast[d]*. National University of Singapore.

Li, V.C. & Maalej, M. (1996). Toughening in cement based composites-part ii: Fiber-reinforced cementitious composites. *Journal of Cement and Concrete Composites,* 18 (4), 239-249.

Li, V.C., Mishra, D.K., Naaman, A.E., Wight, J.K., Wu.H.C. & Inada, Y. (1994). On the shear behavior of engineered cementitious composites. *Journal of Advanced Cement Based Materials,* 1 (3), 142-149.

LS-DYNA (2007). *LS-DYNA keyword user's manual*: Livermore Software Technology Corporation (LSTC).

Maalej, M., Quek, S.T. & Zhang, J. (2005). Behavior of hybrid-fiber engineered cementitious composites subjected to dynamic tensile loading and projectile impact. *Journal of Materials in Civil Engineering,* 17 (2), 143-152.

Magallanes, J.M., Wu, Y., Malvar, L.J. & Crawford, J.E. (2010). Recent improvements to release iii of the k&c concrete model. *11th International LS-DYNA Users Conference.* Detroit, USA, 37-48.

Malvar, L.J., Crawford, J.E. & Wesevich, J.W. (1996). *A new concrete material model for dyna3d release ii: Shear dilation and directional rate enhancements.* Defense Nuclear Agency.

Malvar, L.J., Crawford, J.E., Wesevich, J.W. & Simons, D., 1997. A plasticity concrete material model for dyna3d. *International Journal of Impact Engineering,* 19 (9-10), 847-873

Park, D.W., Martin, T., Lee, H.S. & Masad, E. (2005). Characterization of permanent deformation of an asphalt mixture using a mechanistic approach. *KSCE Journal of Civil Engineering,* 9 (3), 213-218.

Polanco-Loria, M., Hopperstad, O.S., Borvik, T. & Berstad, T. (2008). Numercial predictions of ballistic limit for concrete slabs using a modified version of the hjc concrete model. *International Journal of Impact Engineering,* 35, 290-303.

Riedel, W., Kawai, N. & Kondo, K. (2009). Numerical assessment for impact strength measurements in concrete materials. *International journal of Impact Engineering,* 36, 283-293.

Tang, W.-H., Ding, Y.-Q. & Yuan, X.-Y. (2009). The hjc model parameters of an asphalt mixture. *DYMAT 2009 - 9th International Conference on the Mechanical and Physical Behaviour of Materials under Dynamic Loading.* 1419-1423.

Tekalur, S.A., Shukla, A., Sadd, M. & Lee, K.W. (2009). Mechanical characterization of a bituminous mix under quasi-static and high-strain rate loading. *Construction and Building Materials,* 23, 1795-1802.

Wang, F., Lim, C.H. & Soh, T.B. (2010). Explosive testing, numerical and analytical modelling of a modular blast wall system. *The 3rd International Conference on Design and Analysis of Protective Structures.* Singapore, 392-401.

Wu, J. (2012). *Development of advanced pavement materials system for blast load[d]*. National University of Singapore.

Wu, J. & Chew, S.H. (2014). Field performance and numerical modelling of multi-layer pavement system subject to blast load. *Construction and Building Materials,* 52, 177-188.

Zhang, M.H., Sharif, M.S.H. & Lu, G., 2007. Impact resistance of high strength fibre-reinforced concrete. *Magaine of Concrete Research.* 199-210.

Zhang, M.H., Shim, V., P.W, Lu, G. & Chew, C.W. (2005). Resistance of high-strength concrete to projectile impact. *International Journal of Impact Engineering,* 31, 825-841.

Table 1. Parameters from SNB and single element simulation

Parameters	Unit	Value
K_{IC}	MPa • mm ^{½}	12.2
υ	---	0.35
E	MPa	598
G_f	MPa • mm	0.221
w_c	mm	40
G_f/w_c	---	0.00554
f_t	MPa	0.7
b_2	---	0.2

Table 2. Material properties of HSC and ECC

Parameters	Units	HSC	ECC
Young's modulus, E	GPa	33	18
Compressive strength, f_c	MPa	55	64
Tensile strength, f_t	MPa	4.35	5
Poisson's ratio, v	---	0.2	0.22
Density, ρ	kg/m^3	2400	2080

Table 3. Parameters for geosythetics MG-100 and steel materials using a plastic-kinematic model

Parameters	Units	GST	Steel
Young's modulus, E	MPa	500	207000
Yield stress, f_y	MPa	7.5	460
Poisson's ratio, v	---	0.3	0.3
Density, ρ	kg/m^3	1030	7850

Table 4. Material properties of soil mass

Parameters	Units	Value

Density, ρ	kg/m^3	2100
Shear modulus, G	MPa	13.8
Poisson's ratio, v	---	0.3
Cohesion, c	kPa	62
Friction angle, φ	^{o}	26

Table 5. Parameters for interface simulation

Parameters	Unit	Value
Contact type	---	TIEBREAK
Friction coefficient for static	---	0.71
Friction coefficient for dynamic	---	0.56
τ_n	MPa	0.05
τ_s	MPa	1.15
D	mm	10

Table 6. Vertical acceleration of the proposed multi-layer pavement slab

Item	Field trial test	Numerical result	Deviation from field trial test
Max. vertical acceleration (m/s^2)	35,400	38,870	10 %

Table 7. Peak reading for total pressure cell

Item	Field blast test (kPa)	Numerical result (kPa)	Deviation from field trial test
TPC1	Destroyed	13,393	Sensor destroyed as pressure >> range
TPC2	273	267	2 %
TPC3	200	241	20 %

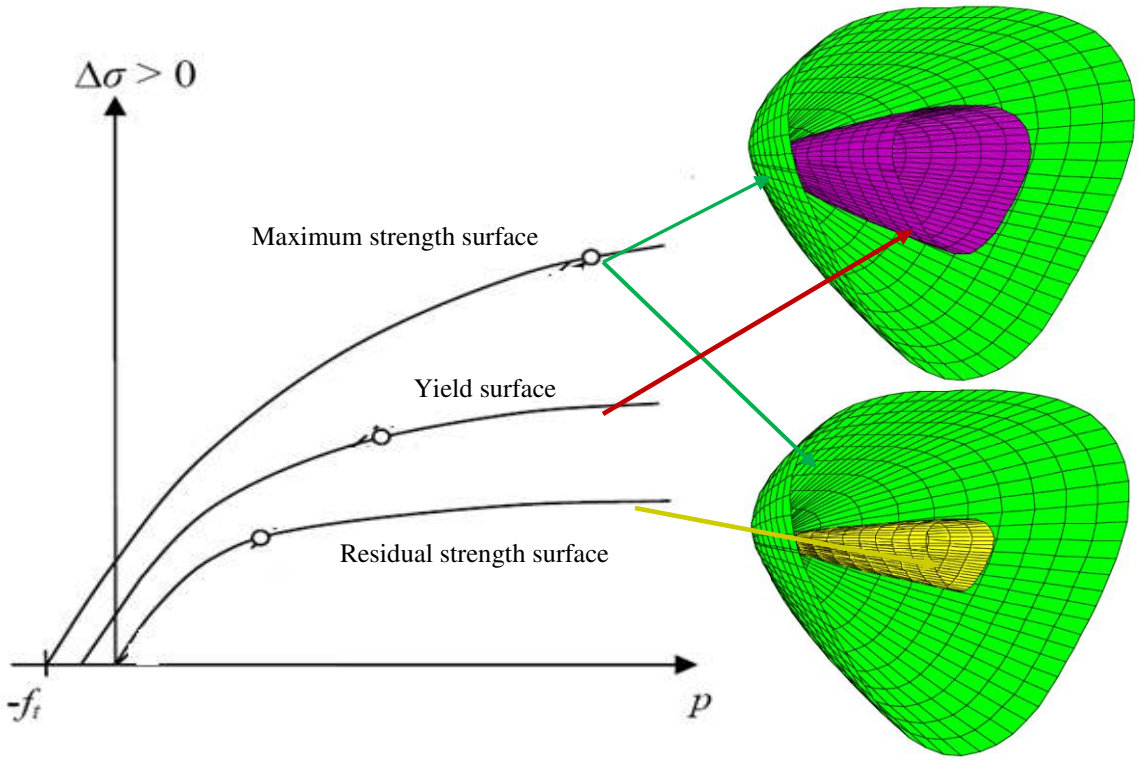

Figure 1. Strength surfaces for MAT72 R3 material model

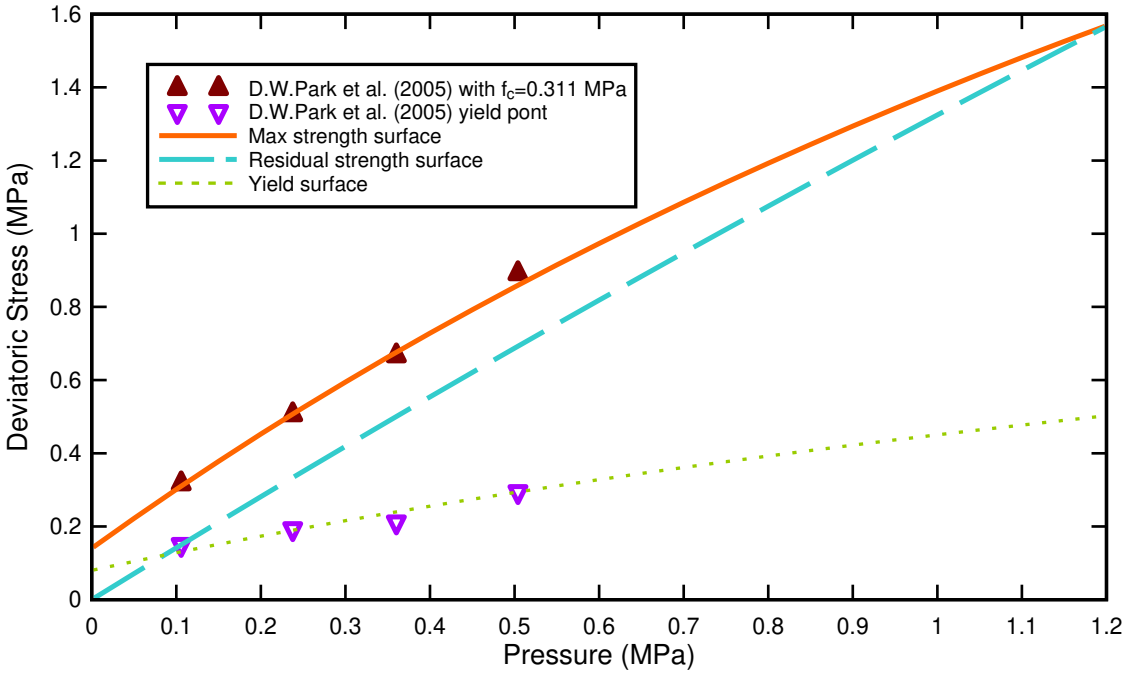

Figure 2. Determination of parameters in MAT 72 R3 from experimental data

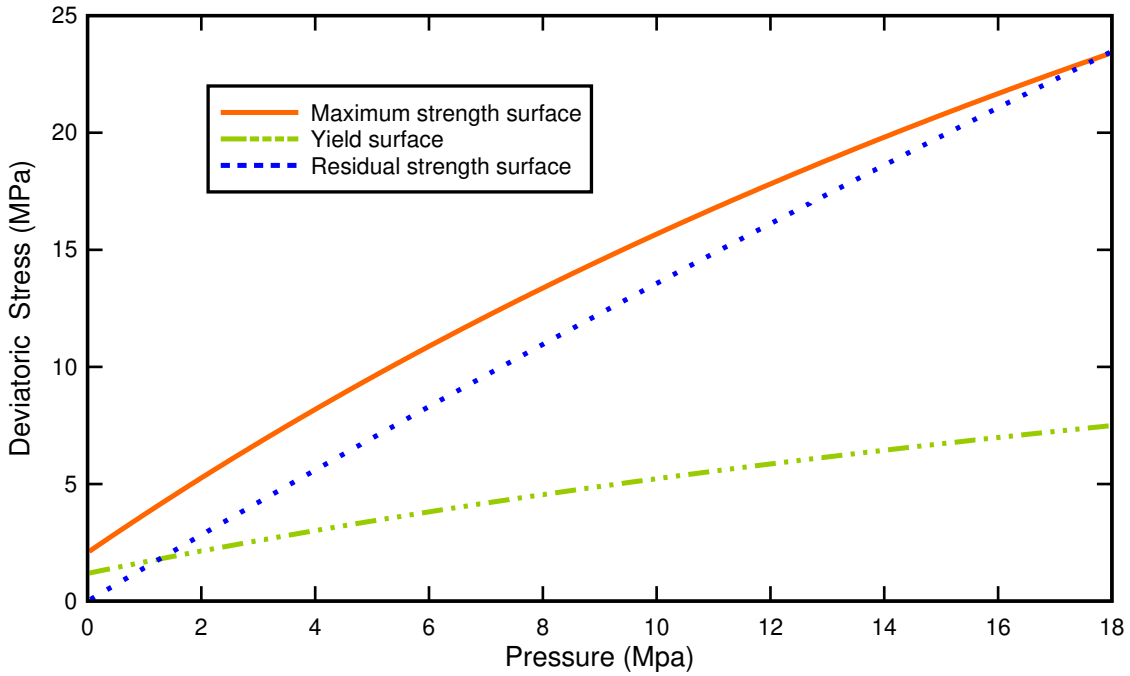

Figure 3. Strength surface for AC with f_c=4.6 MPa

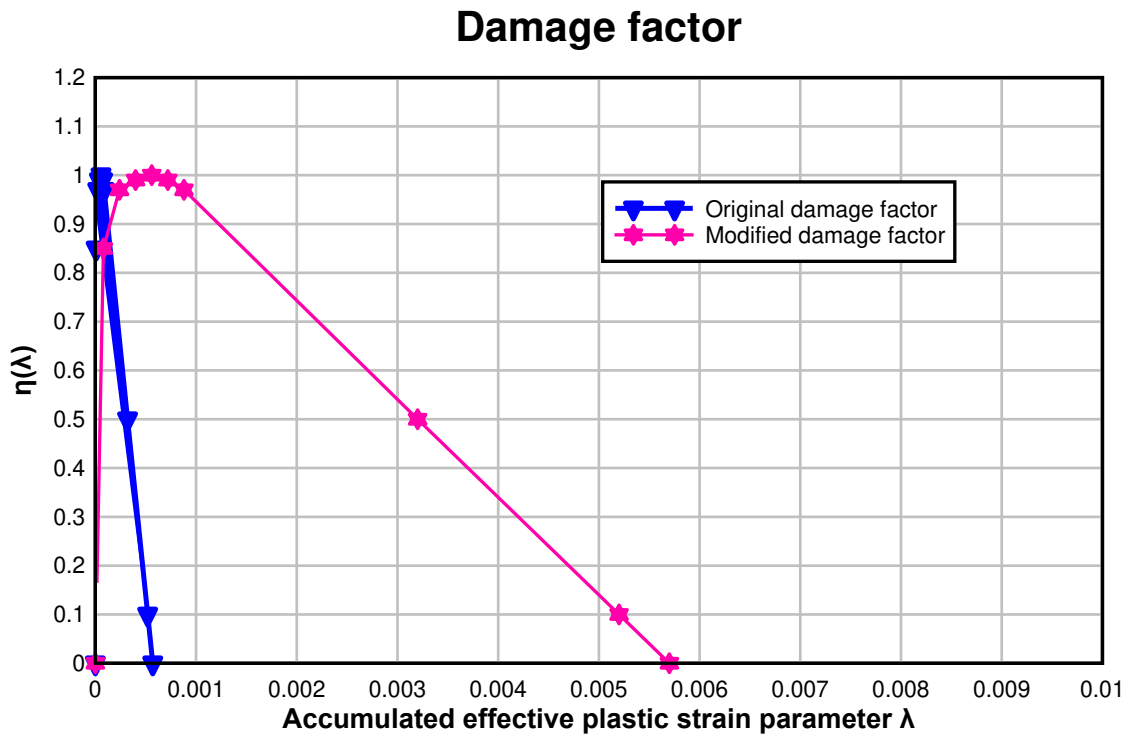

Figure 4. Damage factor used for AC material

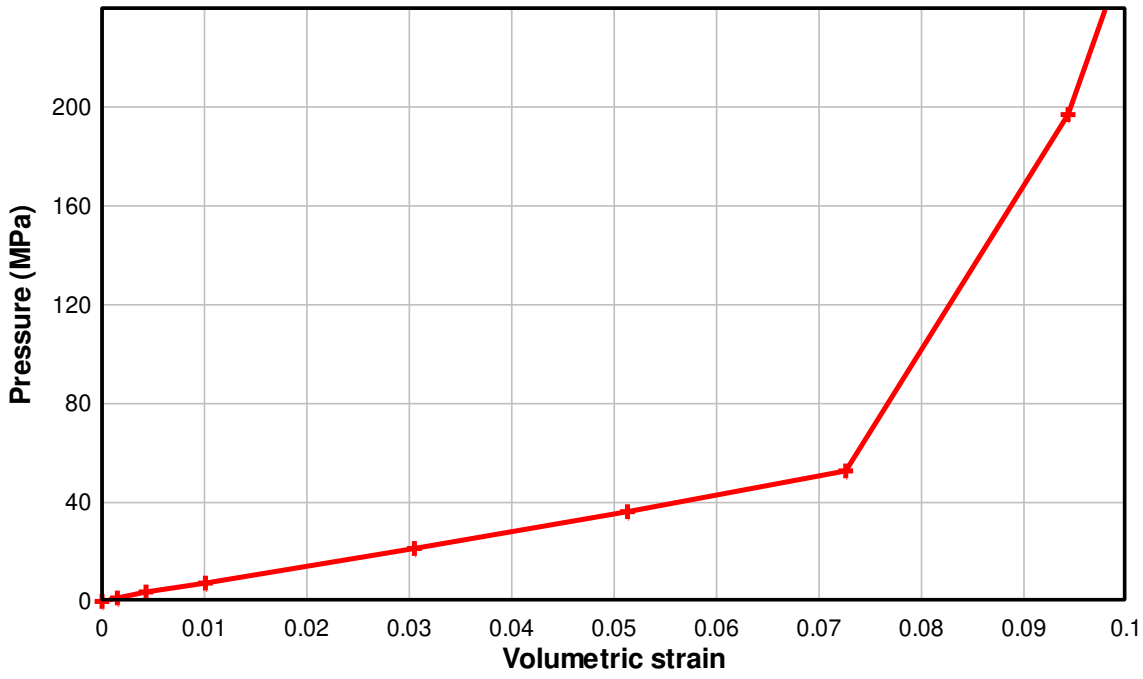

Figure 5. EOS for AC with f_c=4.6 MPa

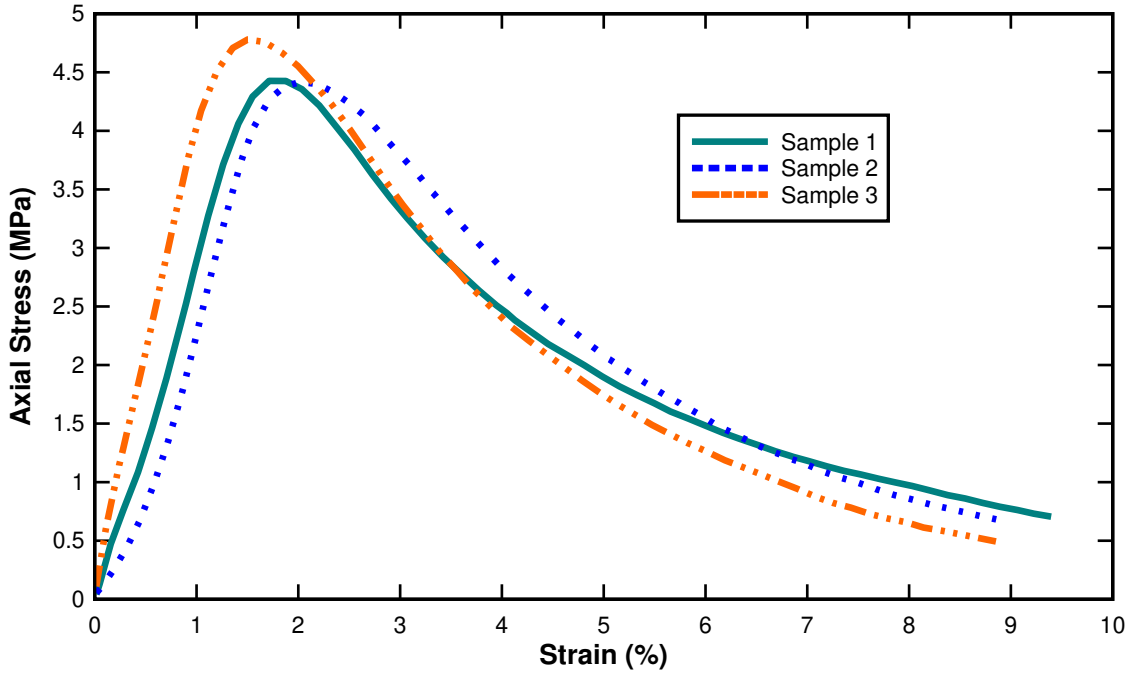

Figure 6. Stress-strain curve of uniaxial compressive test for AC

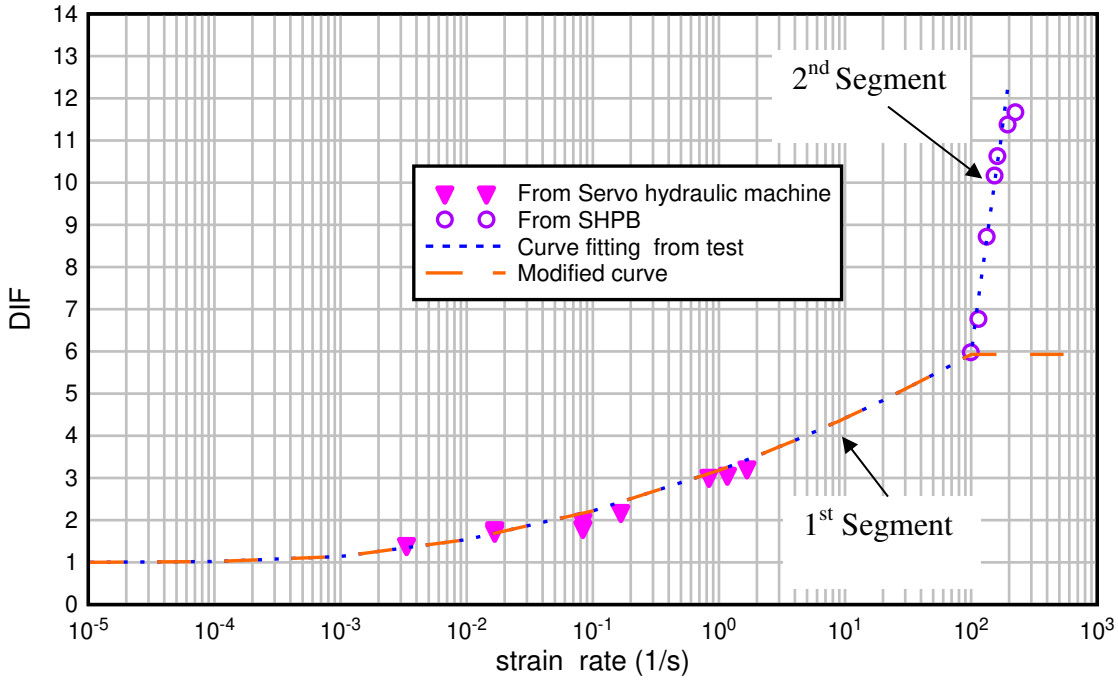

Figure 7. Compressive DIF curve versus different strain rate from lab test

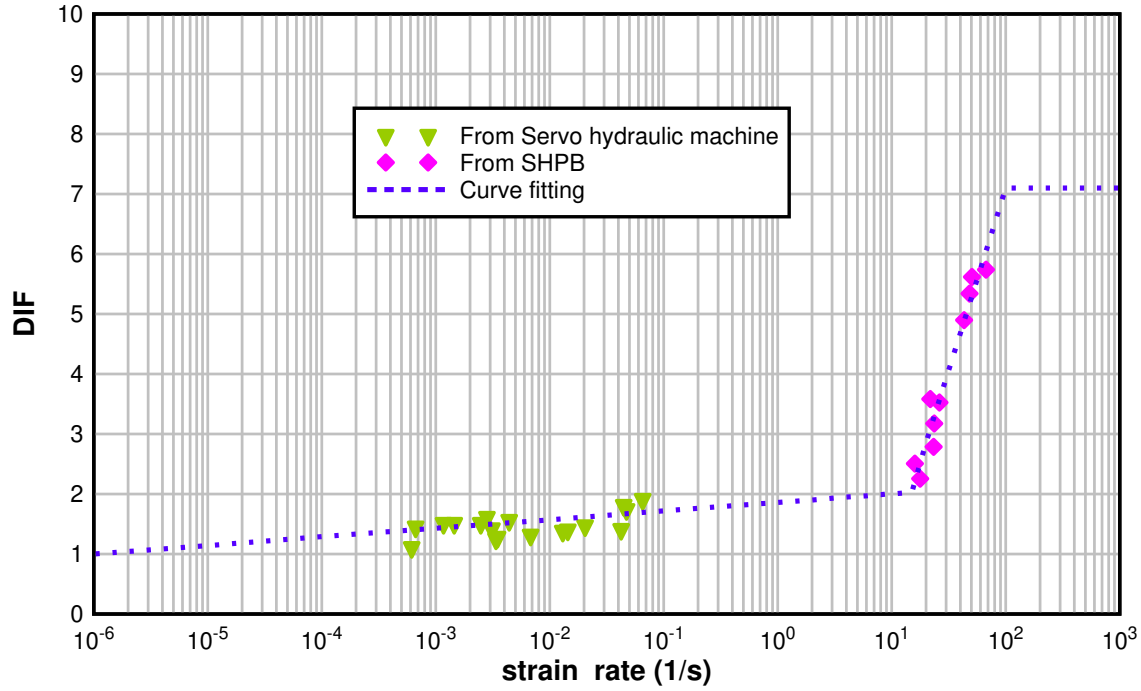

Figure 8. Tensile DIF curve versus different strain rate from lab test

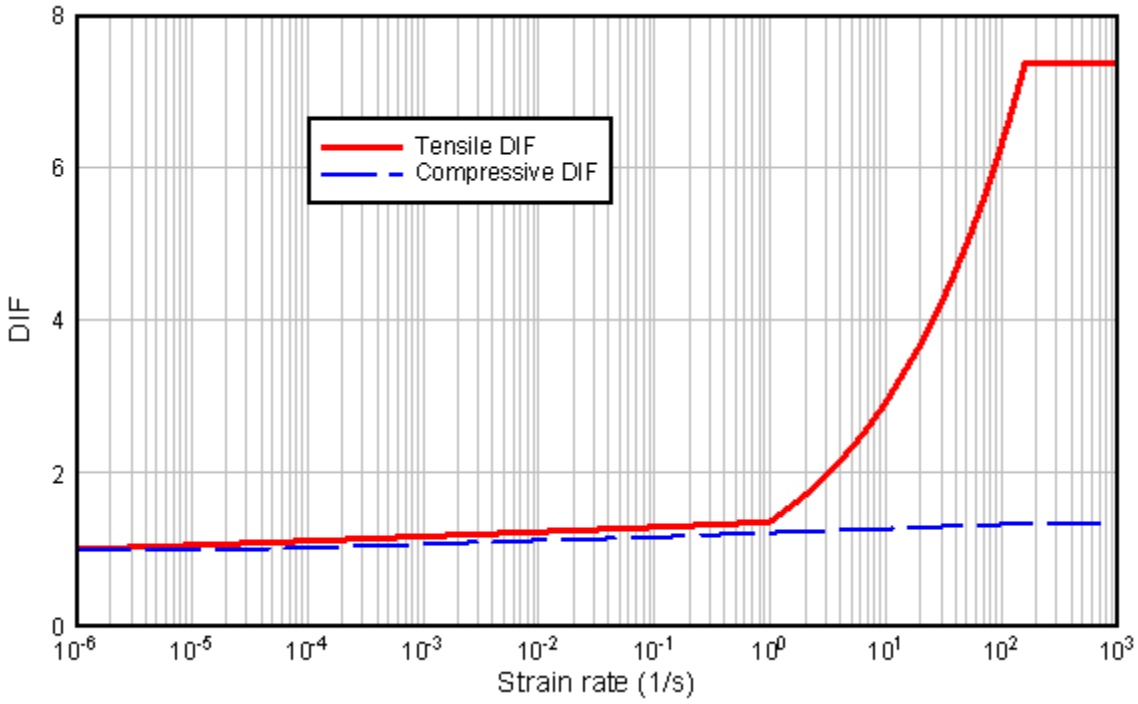

Figure 9. Tensile and compressive DIF curve used in numerical model for HSC with f_c=55 MPa

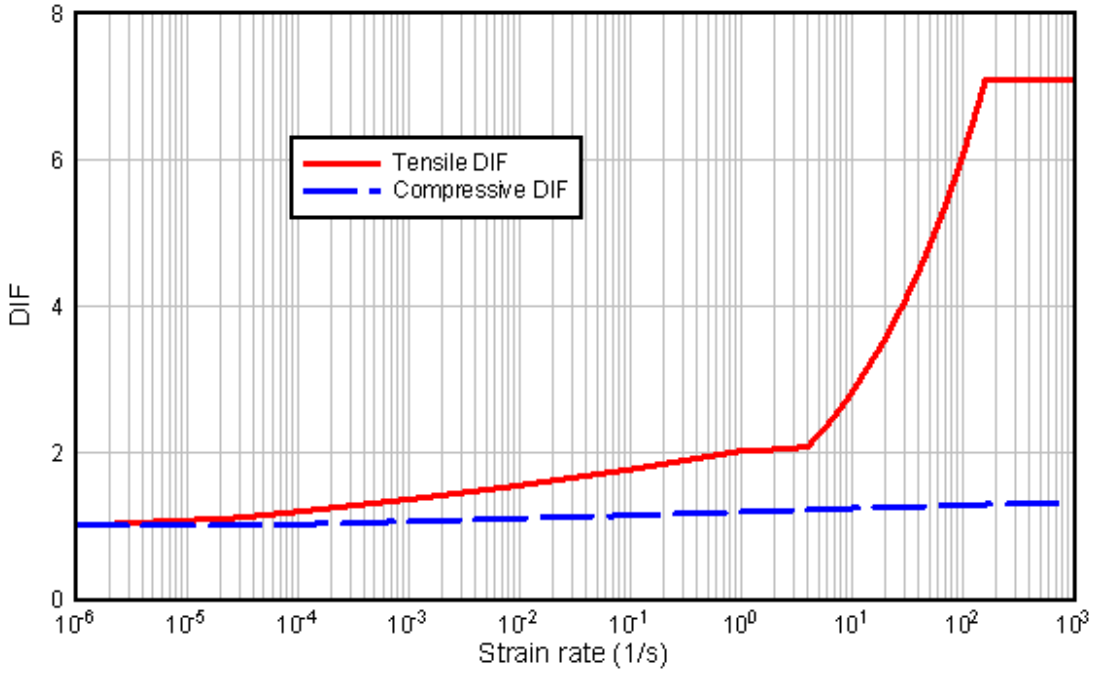

Figure 10. Tensile and compressive DIF curve used in numerical model for ECC with f_c=64 MPa

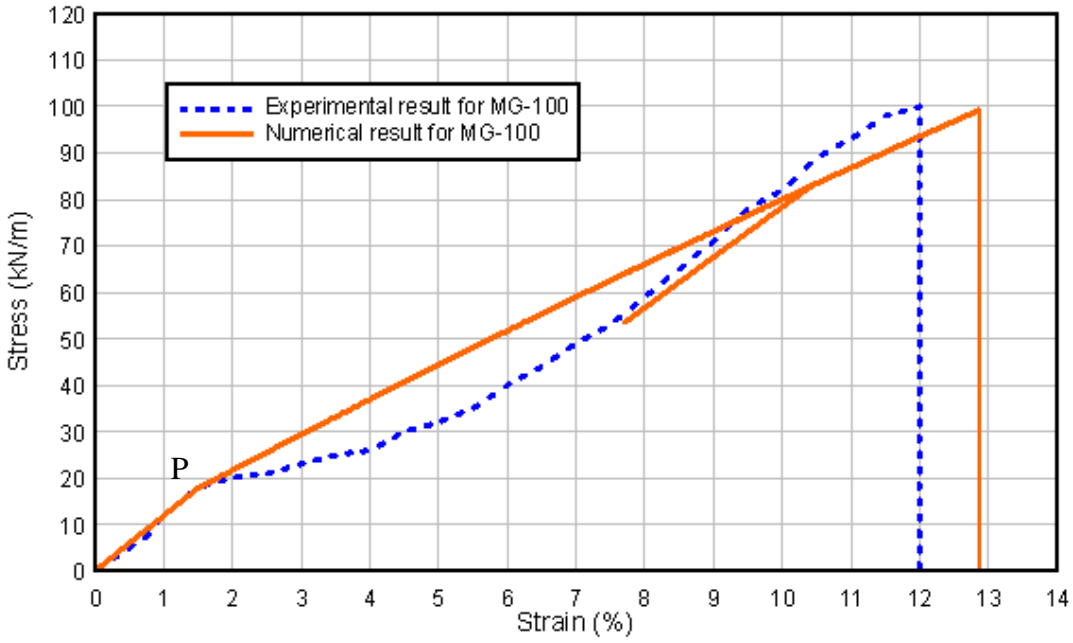

Figure 11. Load strain relationship of MG-100 GST reinforcements

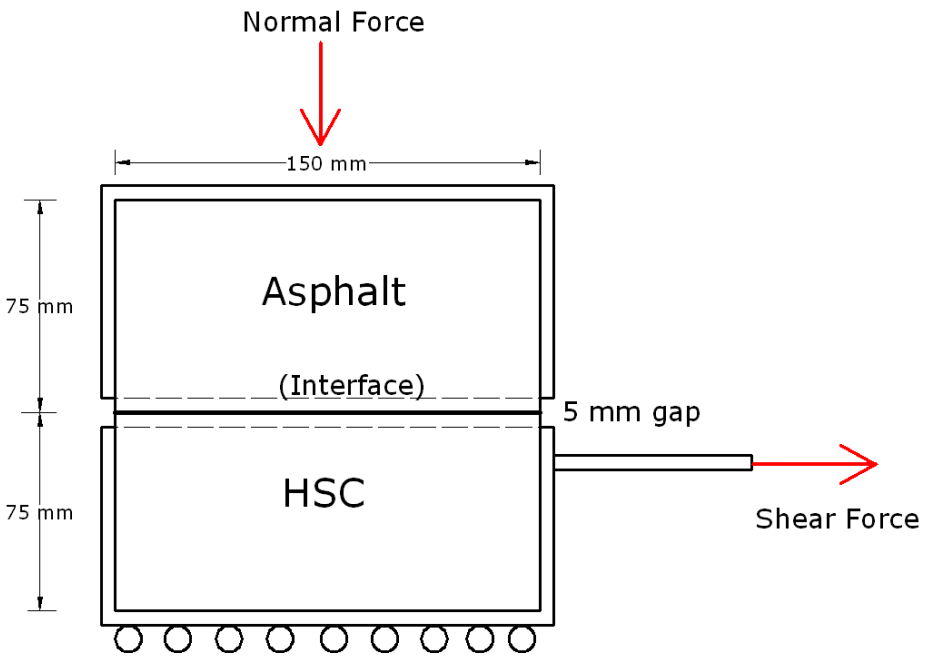

(a)

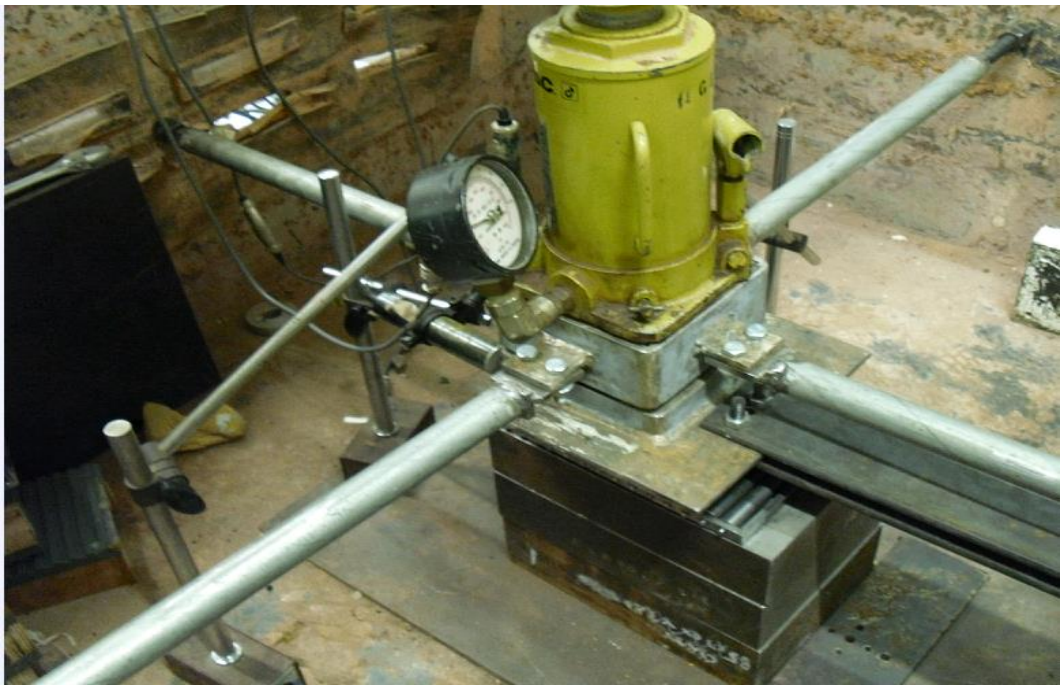

(b)

Figure 12. Configuration of direct shear test, (a) Sketch of direct shear test, and (b) Apply normal force by hydraulic jack

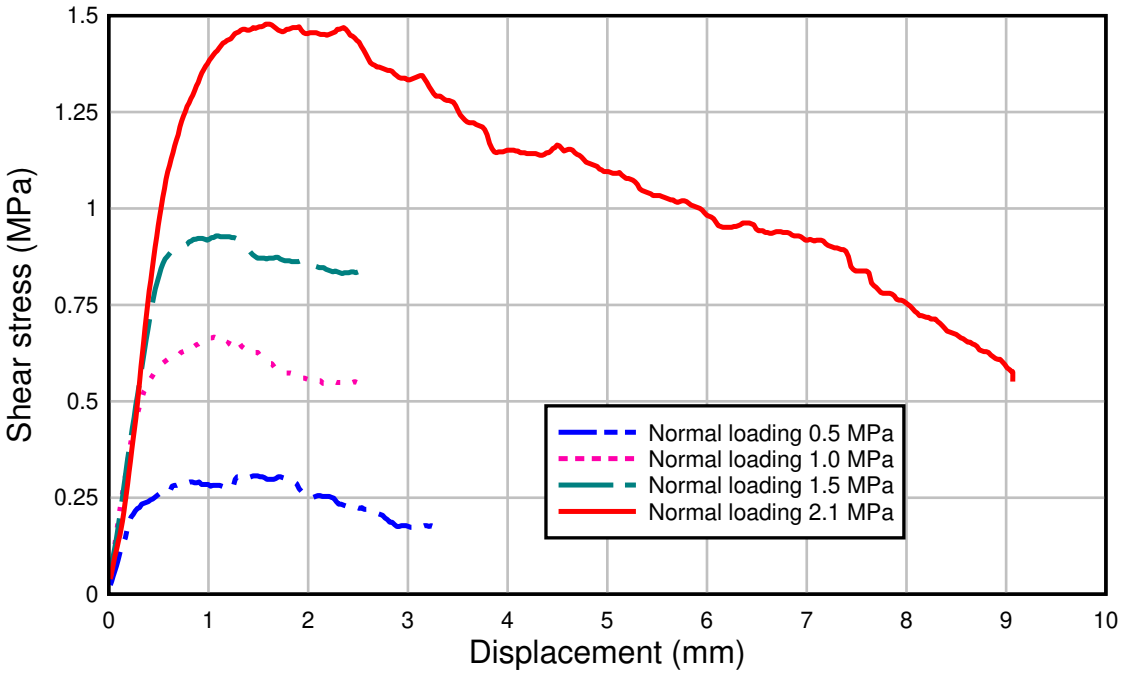

Figure 13. Shear stress and displacement in direct shear test

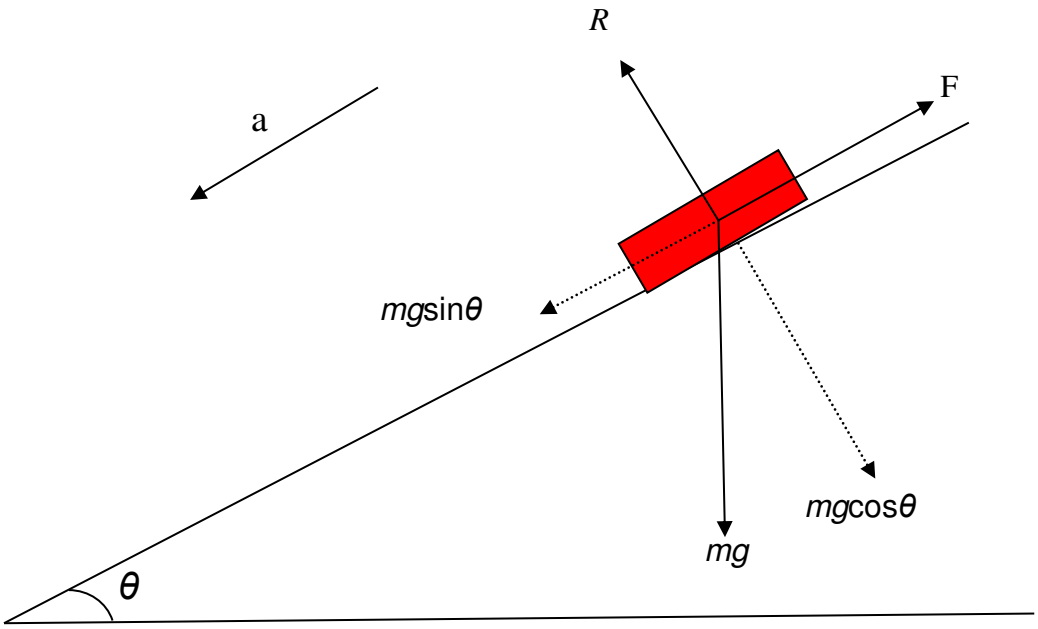

Figure 14. Tilt table test theoretical analysis

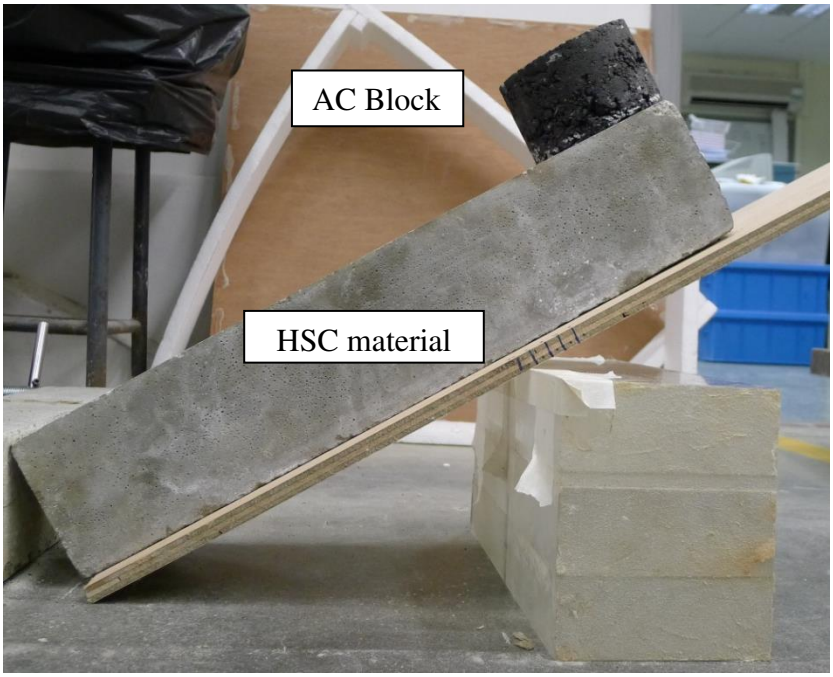

(a)

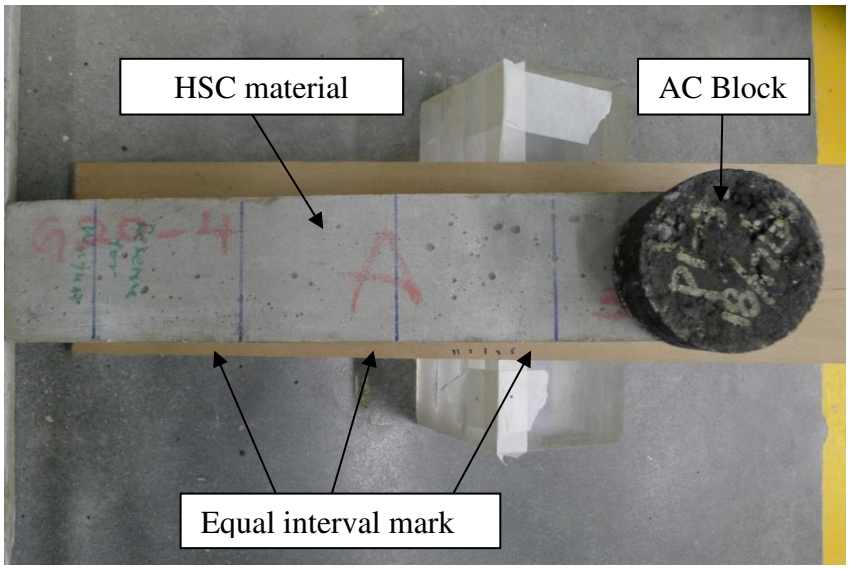

(b)

Figure 15. Set up for tilt table test: (a) Side view, and (b) Plan view

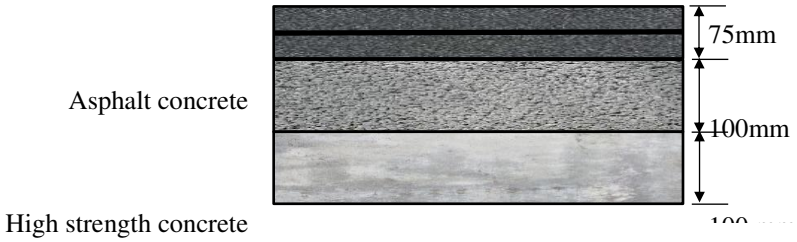

Figure 16. Configuration of the innovative SHS multi-layer pavement composite used in field blast test

Figure 17. Completed SHS multi-layer pavement slab with anchoring at site

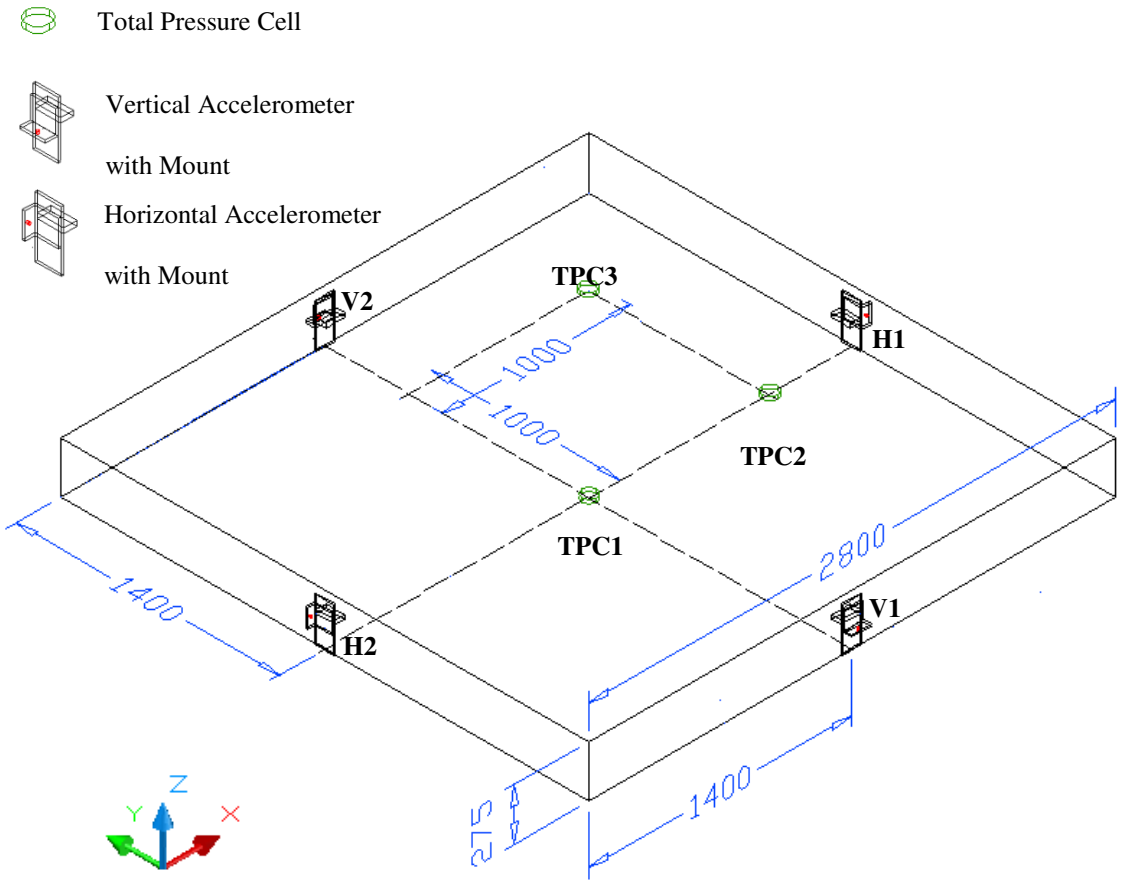

Figure 18. Layout of instrumentation for blast test

Figure 19. Damage of the multi-layer pavement after blast load with top layer AC in place

Figure 20. Damage of proposed multi-layer pavement after blast (after removing AC layer)

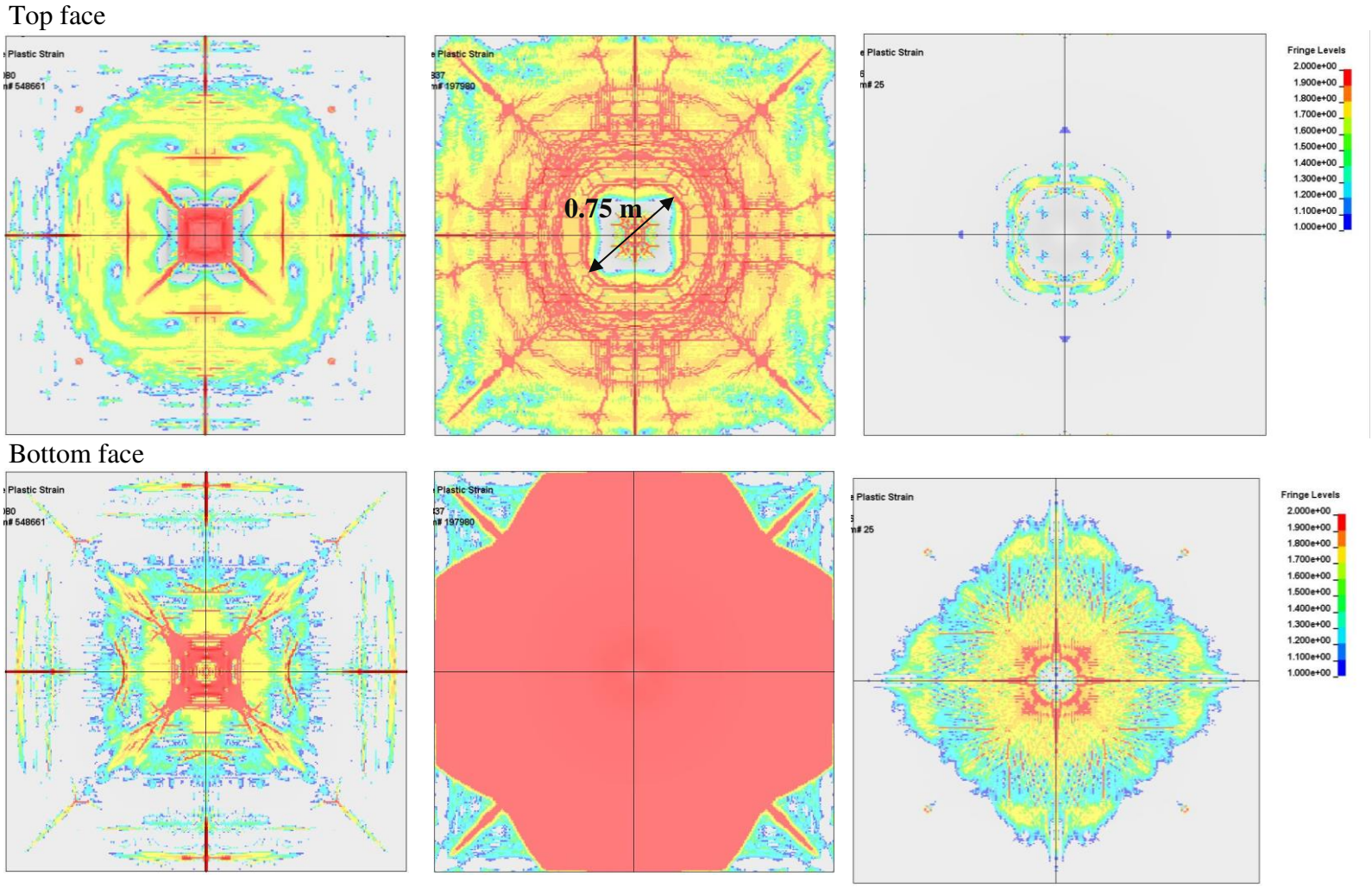

(a) AC layer (b) HSC layer (c) ECC layer

Figure 21. Damage pattern for each layer of proposed multi-layers pavement